Journal of Physics: Conference Series **625** (2015) 012031 doi:10.1088/1742-6596/625/1/012031

# Large-eddy simulation of the diurnal variation of wake flows in a finite-size wind farm

**Mahdi Abkar, Ahmad Sharifi, Fernando Porté-Agel**

École Polytechnique Fédérale de Lausanne (EPFL), Wind Engineering and Renewable Energy Laboratory (WiRE), EPFL-ENAC-IIE-WIRE, CH-1015 Lausanne

E-mail: fernando.porte-agel@epfl.ch

**Abstract.** In this study, large-eddy simulation (LES) is used to study the evolution of the wind-turbine wakes and their effects on power losses inside an idealized finite-size wind farm in the course of a full diurnal cycle. In the LES, turbulent subgrid-scale stresses are modeled using tuning-free Lagrangian scale-dependent dynamic models, while the turbine-induced forces are parameterized using a dynamic actuator disk model with rotation. The simulation results show a strong effect of atmospheric stability on the wind farm wakes and associated power losses. During the night, the relatively low turbulence intensity of the ambient ABL flow results in a relatively slow rate of entrainment of momentum into the wake and, consequently, a slow wake recovery. In contrast, during the day the positive buoyancy flux and associated turbulence production lead to a relatively high turbulence level in the background ABL flow, which enhances turbulent mixing and wake recovery. As a result, the averaged power deficit in the wind farm is found to increase with increasing thermal stability. In particular for that day, the averaged power deficit increased from 28% under the most convective condition to about 57% under the most stable condition.

## 1. Introduction

In a wind farm, with a relatively small spacing between turbines, the wind speed in the turbine wakes does not recover to its upstream unperturbed value. Hence, the wakes from upstream turbines impact the performance of downstream turbines. Any mechanism that changes the recovery rate of wake flow can increase or decrease the significance of this impact as the greater loss of power production in the downstream turbines is associated with slower rate of wake recovery. In several studies, it has been shown that besides land or sea surface characteristics such as the roughness and topography, thermal stratification has an important effect on the wind-turbine wakes and the performance of wind farms (e.g. [1, 2, 3, 4, 5]). For instance, Zhang et al. [6] carried out wind-tunnel experiments of the down-scaled wind-turbine models to investigate the effect of thermal stability on wind-turbine wakes under the convective and neutral conditions. They found a smaller velocity deficit (about 15% at the wake center) in the CBL compared with the wake of the same wind turbine in the neutral boundary layer. Barthelmie and Jensen [7] analyzed power output data from Nysted wind farm and found reduced power efficiency in the wind farm under stable conditions. Churchfield et al. [8] used LES (Open-FOAM) to study the effects of unstable stratification on the power deficit as well as fatigue loads on a wind turbine placed downstream of another turbine. They concluded that under unstable stratification, the power deficit was 15-20% lower in comparison with neutral condition; also fatigue loads were

greater. Despite the valuable insights provided by the above-mentioned studies, a number of key questions remain regarding the impact of thermal stability on the dynamics of turbine wakes and its effects on the power deficit inside finite-size wind farms.

Here, an in-house LES code (the WiRE LES) is used to investigate the effects of atmospheric stability changes through a full diurnal cycle on the performance of a finite size wind farm and the wake flow structure, dynamics and associated power losses. In the WiRE LES, the SGS turbulent fluxes are parameterized using tuning-free Lagrangian scale-dependent dynamic models [9] and the turbine-induced forces are modelled using the rotational dynamic actuator disk model [10, 11]. A short introduction of the LES framework is presented in Section 2. Section 3 presents the the LES result for precursor simulation of the ABL flow in through the wind turbines. Finally, a summary and conclusions are provided in Section 4

## 2. Large-Eddy Simulation Framework

### *2.1. LES Governing Equations*

LES solves the filtered continuity equation, the filtered Navier-Stokes equations (written here using the Boussinesq approximation), and the filtered transport equation for potential temperature:

$$\frac{\partial \widetilde{u}_i}{\partial x_i} = 0,$$

$$\frac{\partial \widetilde{u}_i}{\partial t} + \widetilde{u}_j \frac{\partial \widetilde{u}_i}{\partial x_j} = -\frac{\partial \widetilde{p}^*}{\partial x_i} - \frac{\partial \tau_{ij}^d}{\partial x_j} + \delta_{i3} g \frac{\widetilde{\theta} - \langle \widetilde{\theta} \rangle}{\theta_0} + f_c \varepsilon_{ij3} (\widetilde{u}_j - G_j) - \frac{f_i}{\rho}, \tag{1}$$

$$\frac{\partial \widetilde{\theta}}{\partial t} + \widetilde{u}_j \frac{\partial \widetilde{\theta}}{\partial x_j} = -\frac{\partial q_j}{\partial x_j},$$

where the tilde represents a spatial filtering at scale $\widetilde{\Delta}$, $t$ is time; $\widetilde{u}_i$ is the instantaneous resolved velocity in the $i-$direction (with $i = 1, 2, 3$ corresponding to the streamwise ($x$), spanwise ($y$) and vertical ($z$) directions, respectively); $\widetilde{\theta}$ denotes the resolved potential temperature; $\theta_0$ is the reference temperature, the angle brackets represent a horizontal average; $G$ is the geostrophic wind; $g$ refers to the gravitational acceleration; $\delta_{ij}$ is the Kronecker delta; $\tilde{p}^* = \widetilde{p}/\rho + \frac{1}{3}\tau_{kk}$ is the modified kinematic pressure; $f_i$ is a body force (per unit volume) used to model the effect of the turbine on the flow, $\rho$ is the fluid density; $q_j$ denotes the SGS heat flux; $\tau_{ij}$ represents the kinematic SGS stress; and $\tau_{ij}^d$ is its deviatoric part. Note that $\tau_{ij}^d$ and $q_j$ are unknown and need to be parameterized as a function of filtered (resolved) fields. Regarding the SGS turbulent fluxes, the SGS stress and the SGS heat flux are computed with eddy-viscosity and eddy-diffusivity models, respectively, as follows [12]:

$$\tau_{ij}^d = -2\widetilde{\Delta}^2 C_S^2 |\widetilde{S}| \widetilde{S}_{ij}, \qquad q_j = -2\widetilde{\Delta}^2 C_S^2 Pr_{sgs}^{-1} |\widetilde{S}| \frac{\partial \widetilde{\theta}}{\partial x_j}, \tag{2}$$

where $\tilde{S}_{ij} = (\partial \tilde{u}_i/\partial x_j + \partial \tilde{u}_j/\partial x_i)/2$ is the resolved strain-rate tensor whose magnitude is $|\widetilde{S}|$. $C_S$ and $C_S^2 Pr_{sgs}^{-1}$ are the Smagorinsky and the lumped coefficients, respectively, where $Pr_{sgs}$ is the SGS Prandtl number. In this study, we use Lagrangian scale-dependent dynamic models [9] to compute the local optimized value of the model coefficients without any *ad hoc* tuning. More details can be found in Porté-Agel et al. [13], Porté-Agel [14], and Stoll and Porté-Agel [9].

To parameterize the turbine-induced forces, the actuator-disk model with rotation [15] is used. Through this model, the aerodynamic forces are determined using the lift and drag characteristics of the airfoil type as the well as the local flow conditions. Figure 1 shows a cross-sectional element of radius $r$ in the $(\theta, x)$ plane, where $x$ is the axial direction. Different forces, velocities and angles are shown in this figure. $V_x = V_x(r, \theta)$ and $V_\theta = V_\theta(r, \theta)$ are axial

and tangential velocities of the incident flow at the blades, respectively, in the inertial frame of reference. The local velocity relative to the rotating blade is defined as $V_{rel} = (V_x, \Omega r - V_\theta)$, where $\Omega$ is the turbine angular velocity. The angle of attack is defined as $\alpha = \varphi - \gamma$, where $\varphi = \tan^{-1}(V_x/(\Omega r - V_\theta))$ is the angle between $V_{rel}$ and the rotor plane and $\gamma$ is the local pitch angle. To determine the forces acting on the rotor disk, we consider an annular area of differential size $dA = 2\pi r dr$. The resulting force per unit rotor area is given by:

$$\mathbf{f}_{disk} = \frac{d\mathbf{F}}{dA} = \frac{1}{2}\rho V_{rel}^2 \frac{Bc}{2\pi r}(C_L \mathbf{e}_L + C_d \mathbf{e}_D), \tag{3}$$

where $B$ is the number of blades, $C_L = C_L(\alpha, Re_c)$ and $C_D = C_D(\alpha, Re_c)$ are the lift and drag coefficients, respectively, $Re_c$ is the Reynolds number based on relative velocity and chord length, $c$, and $\mathbf{e}_L$ and $\mathbf{e}_D$ denote the unit vectors in the directions of the lift and the drag, respectively. Through the simulation, the tangential ($V_\theta$) and the axial ($V_x$) velocities at the rotor plane are known. Hence, the local velocity relative to the rotating blade ($V_{rel}$) and the angle of attack $\alpha = \varphi - \gamma$ can be computed. Then, the resulting force is obtained using Equation 3.

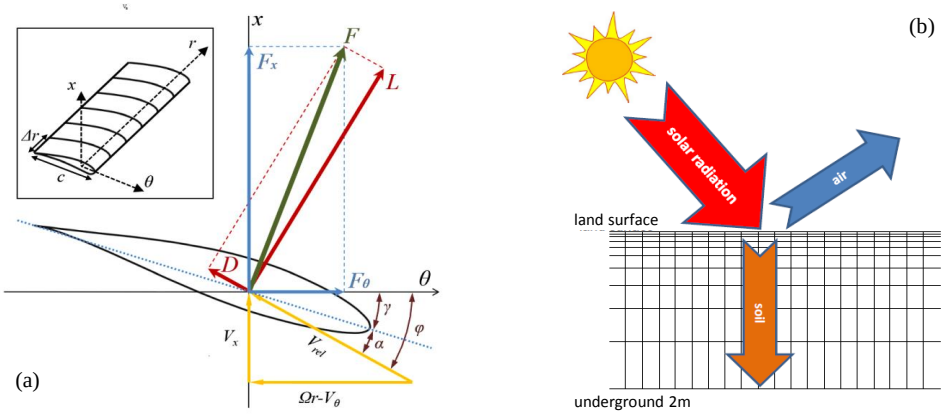


**Figure 1.** (a) A cross-sectional airfoil element. (b) schematic of energy balance, and structured grid for soil showing a depth of 2[m] using a logarithmic spacing in vertical direction.

*2.2. Numerical Setup*

The LES code used in this study is a modified version of the one described by Albertson and Parlange [16], Porté-Agel et al. [13], Stoll and Porté-Agel [9], Wu and Porté-Agel [15], and Ablar and Porté-Agel [17]. In the code, the computational domain is broken uniformly into $N_x \times N_y \times N_z$ grid points with a spatial resolution of $\Delta x \times \Delta y \times \Delta z$ in the streamwise, spanwise and wall-normal directions, respectively.The grid planes are staggered in the $z-$direction, with the first vertical velocity plane on the surface, and the first horizontal velocity plane $\Delta_z/2$ from the surface. The vertical derivatives are approximated with second-order central differences and the horizontal directions are discretized pseudo-spectrally which requires periodic boundary conditions. Full dealiasing of the nonlinear terms is obtained by padding and truncation according to the 3/2 rule [18]. The time advancement is carried out using a second-order-accurate Adams-Bashforth scheme [19]. The upper boundary condition consists of a stress/flux-free condition. At the bottom surface, the standard formulation based on local application of Monin-Obukhov similarity theory [20] is used. Although this theory was developed for mean quantities, it is a common practice in LES of atmospheric flows to compute the instantaneous filtered surface momentum flux [21, 22] as follows, $\tau_{i3}|_w = -u_*^2 \frac{\tilde{u}_i}{\tilde{u}_r} = -(\frac{\tilde{u}_r \kappa}{\ln(z/z_o) - \Psi_M})^2 \frac{\tilde{u}_i}{\tilde{u}_r}$, where

$\tau_{i3}|_w$ is the instantaneous local wall stress; $u_*$ is the friction velocity; $z_o$ is the aerodynamic surface roughness; $\kappa$ is the von Kármán constant; and $\tilde{u}_r$ is the local filtered horizontal velocity at the first level $z = \Delta z/2$. In a similar manner, the surface heat flux is computed as, $q_3|_w = \frac{u_*\kappa(\theta_s - \tilde{\theta})}{\ln(z/z_{ot}) - \Psi_H}$, where $\theta_s$ is the surface (ground level) potential temperature, $z_{ot}$ is the surface roughness for potential temperature and is set to 10% of the aerodynamic surface roughness;and $\tilde{\theta}$ denotes the resolved potential temperature at the first vertical level. $\Psi_M$ and $\Psi_H$ are the stability corrections for momentum and heat, respectively, and are defined as follows [23, 24]:

$$\Psi_M = \begin{cases} -4.7\frac{z}{L} & \text{for stable conditions,} \\ 2\ln[\frac{1}{2}(1+x)] + \ln[\frac{1}{2}(1+x^2)] - 2\tan^{-1}[x] + \frac{\pi}{2} & \text{for unstable conditions,} \end{cases} \tag{4}$$

and

$$\Psi_H = \begin{cases} -7.8\frac{z}{L} & \text{for stable conditions,} \\ 2\ln[\frac{1}{2}(1+x^2)] & \text{for unstable conditions,} \end{cases} \tag{5}$$

where $L = -(u_*^3\theta_0)/(\kappa g q_3|_w)$ is the local Obukhov length, $\theta_0$ is the reference temperature and is set to $\theta_0 = 293K$, and $x = (1 - 15\ z/L)^{1/4}$.

The LES of the diurnal cycle of ABL is performed over a domain of size 4.8 km $\times$2.4 km $\times$1.6 km discretized into 120 $\times$ 160 $\times$ 160 grid-points. Hence, the spatial resolution is $\Delta_x$ = 40m, $\Delta_y$ = 15m, and $\Delta_z$ = 10m. It is worth mentioning that based on previous grid-resolution sensitivity results [15, 25], the grid resolution used in this study is well suited for the LES framework to account for the most significant characteristics of wind-turbine wakes. The boundary layer is driven by an imposed, uniform geostrophic wind ($G$) of 10 m/s. The Coriolis parameter is $f_c = 1 \times 10^{-4}$ rad/s corresponding to a latitude of about $43.3^o$. The aerodynamic surface roughness $z_o$ is set to 0.05 m, and the reference potential temperature is $\theta_0$ = 293 K. In this study, in order to determine the land-surface temperature and surface heat flux, we adopt a surface thermal energy balance approach along with 10 levels of soil temperature to a depth of 2 m using a logarithmic spacing, as shown in Fig. 1b. A similar method has been used by Deardorff [26], but in this study we release the assumption of horizontally homogeneous, and solve a three-dimensional heat transfer equation for the soil as: $\frac{\partial\widetilde{\theta}}{\partial t} = \alpha_{soil}\nabla^2\widetilde{\theta}$, where $\alpha_{soil}$ is the soil thermal diffusivity. The simulations are initialized with a constant streamwise velocity $U_g$ = 10 m/s and zero velocity for the spanwise and vertical components. The potential temperature is initialized with a uniform temperature of 293 in the lowest 100 m. In this layer, a very small random perturbations are added to the initial velocity and potential temperature fields. Above this layer, the ABL is set to be laminar with a constant lapse rate of 10 K/km. The initial soil temperature is also uniform and equal to 293 K. The soil is assumed to be dry ground, and its diffusivity is $5.0 \times 10^{-7}$ m$^2$/s (averaged value of desert and concrete [26, 23]). The heat capacity of the soil is $1.3 \times 10^6$ J/m$^3$K [23]. For the surface thermal energy balance, we use the typical profile for the net radiative flux throughout the day [23] as shown in Fig. 2. The simulations are carried out for two full diurnal cycles. To minimize the effects of the initial conditions on the results, our analysis is focused on the second diurnal cycle.

In the simulation of the diurnal ABL flow through the wind farm, 36 Vestas V-80 2MW wind turbines arranged in 6 rows and 6 columns are immersed in the flow. The wind farm is infinite in the spanwise direction as a result of the implicit periodic boundary condition at the spanwise boundaries. Each turbine has a hub height of $h_{hub}$ = 70 m and rotor diameter of $D$ = 80 m. More details on the turbine characteristics can be found in Wu and Porté-Agel [11]. $S_x = 7D$ and $S_y = 5D$ denote the streamwise and spanwise spacings between turbines, respectively. To avoid the downwind flow affecting the flow upwind of the wind turbine due to the periodic boundary conditions, a buffer zone upstream the turbine is employed to adjust the flow from the downwind condition to that of a fully turbulent boundary-layer inflow condition. The inflow

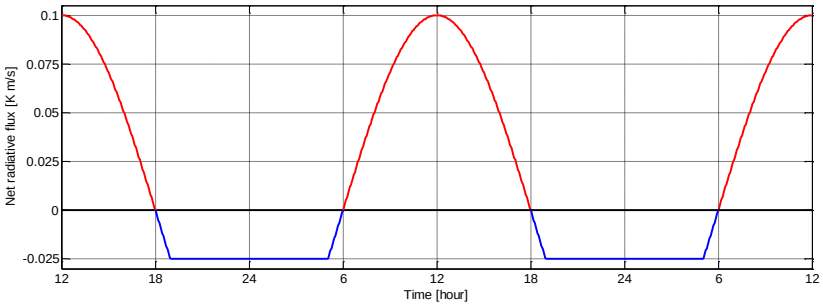


**Figure 2.** Variation of the net radiative flux throughout two full days.

condition is obtained from separate (without turbine) simulations of fully-developed ABL flows over horizontally-homogeneous flat surfaces [27, 15, 28]. In order to ensure that the mean velocity direction is always aligned with the turbine axes at the hub-height level, a control algorithm similar to Sescu and Meneveau [29] is used. In this method a gradual adjustment of the geostrophic wind is applied by adding a source term in the momentum equation. This method allows us to study the effect of wind-farm layout on the ABL flow as well as the power output from wind turbines [30].

## 3. Results

Figure 3 shows the the temporal and spatial evolution of the turbulent kinetic energy (TKE) during the two diurnal cycles. The growth of the boundary layer during the day, due to the entrainment from the overlying inversion layer, is clear in this figure. An strong contrast in the magnitude and vertical extent of the TKE between the daytime and nighttime profiles is also observed. As shown in this figure, the turbulence associated with the convective heating during the day is almost disappeared after the sun set.

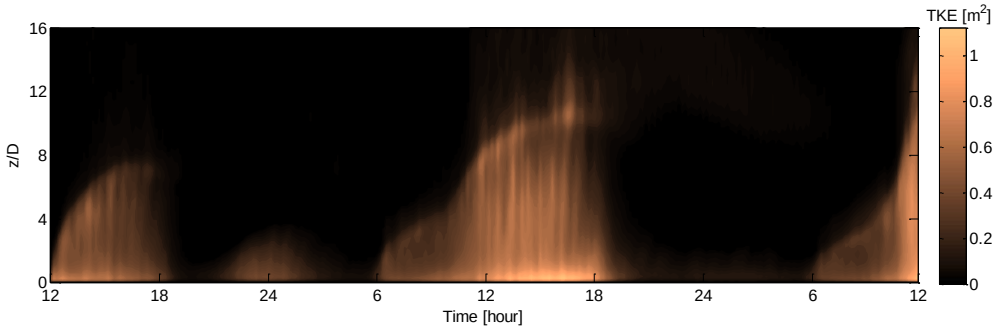


**Figure 3.** Time and space variation of turbulent kinetic energy (TKE) during the 2 full diurnal cycles.

Figure 4 illustrates temporal evolution of the Obukhov length throughout the two full diurnal cycles. The Obukhov length is a common measure to determine the state and strength of the thermal stability in the ABL [31]. In this study, in order to study the wake flow variability in more detail, two time spans (from the second day), based on the magnitude of the Obukhov length, are selected in which the ABL is strongly stable, and strongly unstable.During the the 2nd day, the first hour from $12:00$ to $13:00$ (the time span confined between the two red lines in Fig. 4), with the Obukhov length around $L \cong -95$ m, is selected to study the turbulent ABL

under the condition. Beside that, in the morning of the 2nd day, from 04 : 00 to 05 : 00 (the time span confined between the two blue lines in Fig. 4), the Obukhov length is about $L \cong 76$ m which indicates a strong stability condition in the ABL. As a result, this time span is also selected to study the wake flow under the stable stratification.

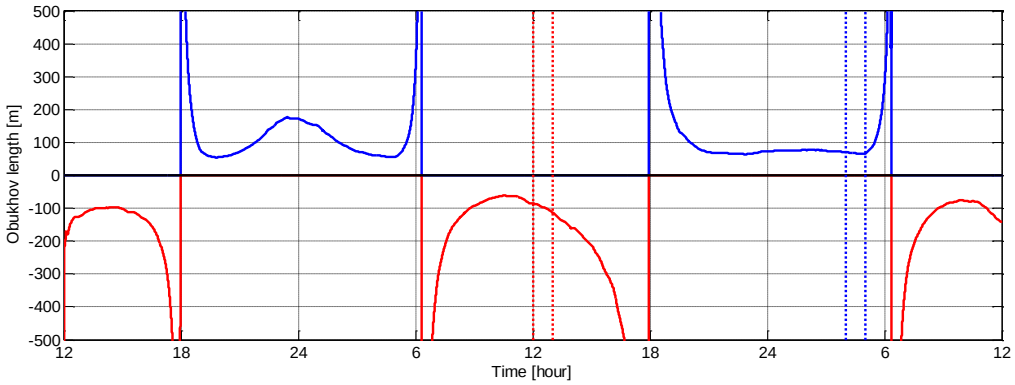


**Figure 4.** Time variation of the Obukhov length in the simulations.

Figures 5a and 5b display vertical profiles of the horizontally-averaged wind velocity magnitude, and wind direction (obtained from the precursor run), respectively, for each case. The blue lines denote the stable case, and the red lines denote the unstable case. As expected, under the stable condition, the mean wind shear is stronger near the surface compared with the convective case (Fig. 5a). It is also clear that, as a result of the Coriolis effects, the wind direction changes with height, resulting in a lateral shear in addition to the vertical shear (Fig. 5b). Especially for the stable condition, the boundary layer is very shallow, which leads to a strong lateral shear. Figure 5c displays vertical profiles of the streamwise turbulence intensity for each case. As seen in this figure, in the case of very stable stratification, the strong negative buoyancy flux acts against the shear production from the surface and decreases the ambient turbulence intensity in comparison with the unstable case. In contrast, during the day, the strong positive buoyancy flux stirs the air above the surface and increases the turbulence intensity significantly. Similarly, the total shear stress in the stable condition is lower compared with the unstable one (Fig. 5d). Figure 5e illustrates vertical profiles of the horizontally-averaged potential temperature for each case. The vertical distribution of horizontally-averaged soil temperature for the two cases is also plotted in Fig. 5f. As shown in this figure, and consistent with the analytical solution (see e.g., [23]), during the day with positive heat flux from the surface soil temperature decays exponentially with depth, and that changes mostly occur within a shallow layer near the surface ($0 - 50$cm).

Figure 6 shows two-dimensional fields of the mean simulated wind velocity in a horizontal $x - y$ plane through the turbine hubs. The normalized velocity through the center of the turbines (at hub height), averaged over all 6 rows of turbines, is also plotted with downwind distance in Fig. 7. In all these figures, the reduction in velocity inside the wakes is clearly visible. Nonetheless, obvious differences are observed between the structure and strength of the wakes in the two stability regimes. Specifically, in the convective boundary layer, with a higher turbulence level, the wake recovers faster. This is due to the fact that, in the unstable condition, the positive buoyancy flux at the surface creates thermal instabilities which enhance the TKE and the turbulent mixing. In contrast, in the stable condition, the negative buoyancy flux at the surface damps the turbulence and, consequently, reduces the turbulent mixing. As a result, it takes a longer distance for the wake to recover. This is consistent with recent experimental and

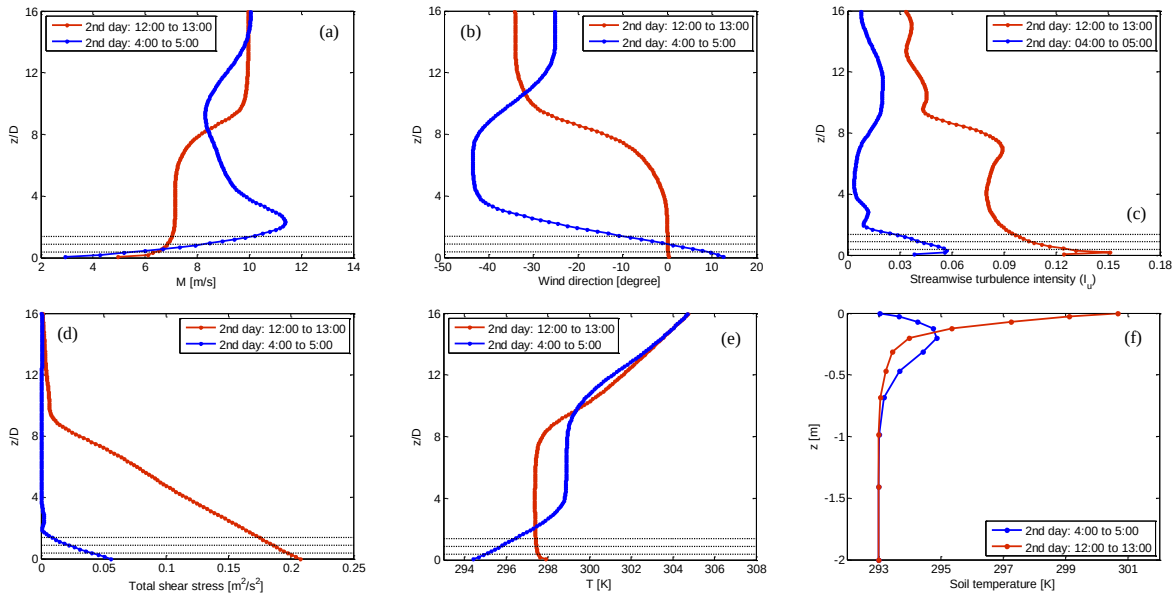


**Figure 5.** Vertical profile of the horizontally-averaged a) wind velocity magnitude, b) wind direction, c) streamwise turbulence intensity, d) total shear stress, e) air potential temperature, and f) soil temperature. The horizontal dotted lines show the top-tip, hub and bottom-tip heights.

numerical studies that show that the recovery rate of the wake from a stand-alone wind turbine recovers faster with decreasing level of stratification [6, 1, 32, 5].

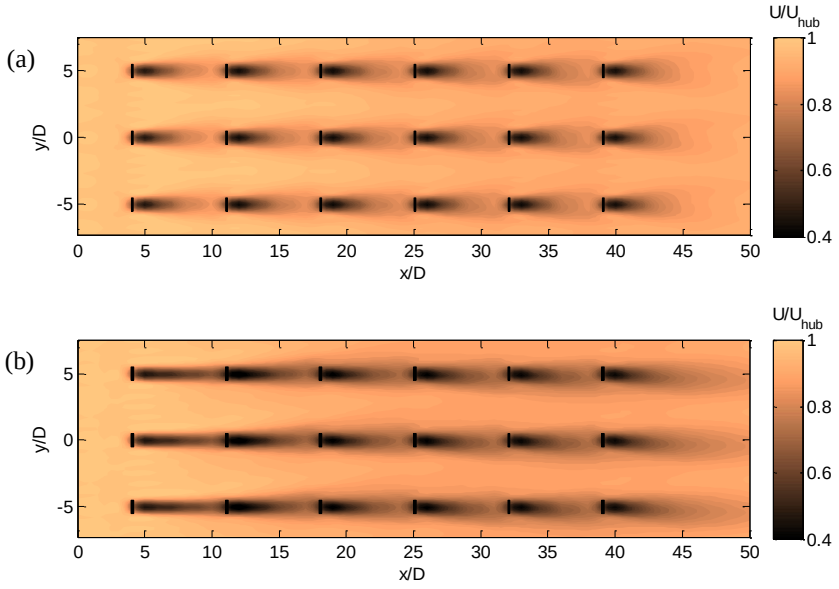


**Figure 6.** Contour plots of the normalized time-averaged streamwise velocity on a horizontal plane at the hub level for: a) the very unstable case (2nd day from 12:00 to 13:00); b) the very stable case (2nd day from 04:00 to 05:00). Only a section of the domain is shown.

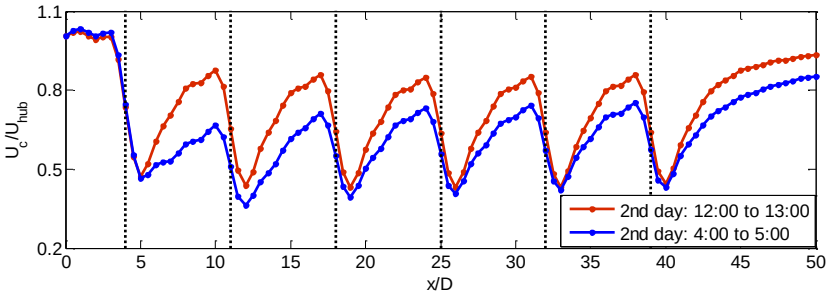


**Figure 7.** Normalized velocity at the center of the turbine with downwind distance. The vertical dotted lines show the location of turbines.

Figure 8 shows contours of the mean streamwise turbulence intensity in the horizontal $x-y$ plane at the hub-height level. As can be seen in the contours, for both stability conditions, the turbulence intensity behind each turbine exhibits a dual-peak pattern with larger values near the two side-tip positions, which is related to the intense production of turbulent kinetic energy associated with the strong shear at those locations. In addition, inside the wind farm, the turbulence intensity is higher in the unstable case in comparison with the stable one. This is mainly related to the fact that, as demonstrated in Fig. 5c, the turbulence level of the incoming wind is higher in the convective condition, which leads to also a larger wake turbulence level compared with the stable counterpart. The higher turbulence intensity at the inflow, and the higher turbulence intensity inside the farm, contribute to the faster recovery of the wakes in the unstable case observed in Figs. 6 and 7. This, in turn, leads to a reduction in the power losses due to wake effects in the wind farm comparing to the stable case, as shown in Fig. 9.

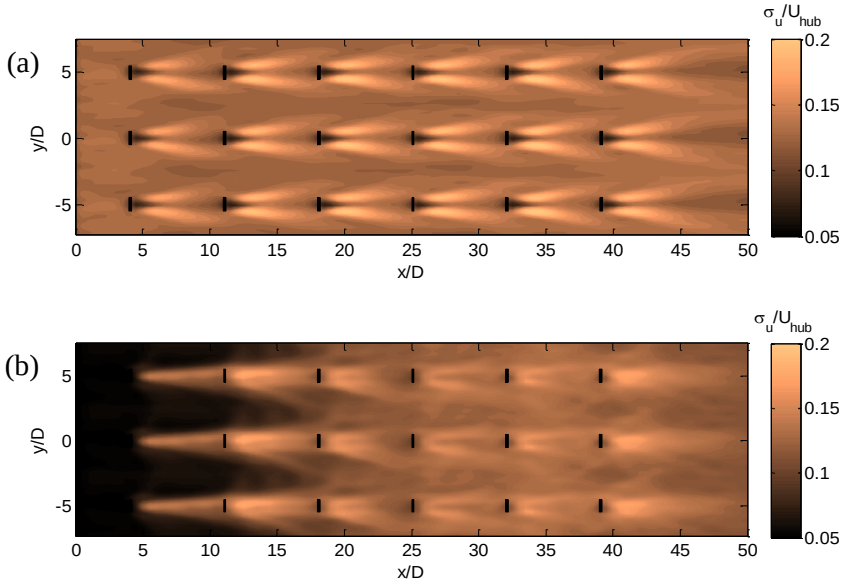


**Figure 8.** Contour plots of the streamwise turbulence intensity on a horizontal plane at the hub level for: a) the very unstable case (2nd day from 12:00 to 13:00); b) the very stable case (2nd day from 04:00 to 05:00). Only a section of the domain is shown.

Figure 10 shows the averaged power deficit throughout the diurnal cycle. As seen in this

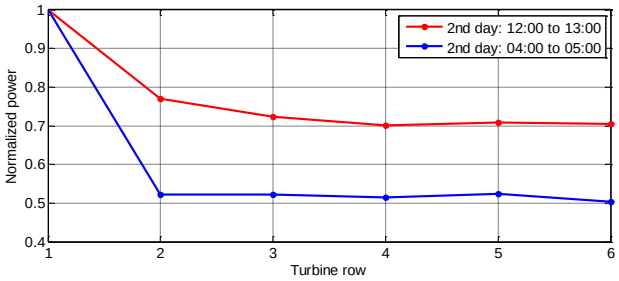


**Figure 9.** Normalized power output from the wind farm as a function of turbine row for the two different stability conditions.

figure, on average, the power deficit is larger during the night in the stable regime compared to the daytime in the convective condition. As mentioned before, this is mainly related to the fact that the turbulence level of the incoming wind to the turbines is larger under the convective condition compared to the stable one. One the other hand, during the night, the turbulence level decreases due to the negative buoyancy fluxes at the surface, the power deficit increases. In particular, for the specific day discussed here, the averaged power deficit increases from 28% under the most unstable condition to about 57% under the most stable case.

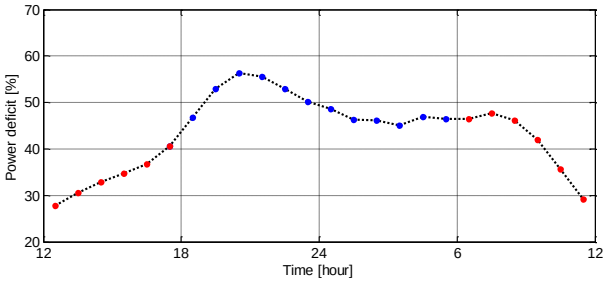


**Figure 10.** Time variation of the averaged power deficit throughout a full diurnal cycle. Each point shows the averaged power deficit over one hour.

## 4. Conclusion

In this study, LES combined with the actuator-disk model is used to study the turbine wakes and their effects on the power loses inside an idealized finite-size wind farm throughout a full diurnal cycle. In the simulations, the tuning-free Lagrangian scale-dependent dynamic models are used to model the SGS fluxes, and the turbine-induced forces (e.g. lift and drag) are parameterized with the dynamic actuator disk model with rotation.

The simulation results demonstrate that, in the absence of turbines, transient nature of the forcing terms such as surface fluxes of momentum and heat significantly affect the structure and dynamics of the ABL in the course of a day. In particular, during the day, when the net radiative flux is positive, the boundary layer grows due to the entrainment from the overlying inversion layer. In addition, the positive buoyancy flux at the surface creates thermal instabilities which enhance the TKE and the turbulent mixing. This enhanced turbulence level diminishes very quickly as the sun sets, and is very small during the nighttime. That is because, the negative surface buoyancy fluxes in the stable condition damps the turbulence, which leads to lower turbulence levels in all three directions. The simulated velocity and temperature fields were then used as inflows to study the the wake flow variability throughout a full day.

The results obtained from the LES of the ABL over a finite-size wind farm show that the atmospheric stability has significant effect of the wind-farm wakes and associated power losses. Specifically, during the day, under the convective condition, the wake recovery is faster compared to the one during the night. This enhancement in the wake recovery rate is mainly related to the higher turbulence level of the incoming wind in the unstable condition, due to positive buoyancy flux and associated turbulence production, which leads to a higher turbulent entrainment flux into the wake. In contrast, during the night, the relatively low turbulence intensity of the ambient ABL flow results in a relatively slow rate of entrainment of momentum into the wake and, consequently, a slow wake recovery. As a result, the averaged power deficit in the wind farm is found to increase with increasing thermal stability. In the particular case considered in this study, the averaged power deficit increased from 28% under the most convective condition to about 57% under the most stable condition.

Future research will address the effect of wind-farm configuration as well as wind direction on the structure and characteristics of wind-turbine wakes and their interaction with the ABL throughout the diurnal cycle.

**Acknowledgements**. This research was supported by the Swiss National Science Foundation (grants 200021-132122 and IZERZ0-142168) and the Swiss Innovation and Technology Committee (CTI) within the context of the Swiss Competence Center for Energy Research FURIES: Future Swiss Electrical Infrastructure. Computing resources were provided by the Swiss National Supercomputing Center (CSCS) under project ID s306.

## References

[1] Hancock P E and Pascheke F 2014 *Boundary-Layer Meteorol.* **151.1** 23–37
[2] Jensen L 2007 *Proc. 2007 EWEC Conf*
[3] Lu H and Porté-Agel F 2011 *Phys. Fluids* **23** 065101
[4] Abkar M and Porté-Agel F 2014 *Renewable Energy* **70** 142–152
[5] Abkar M and Porté-Agel F 2015 *Phys. Fluids* **27** 035104
[6] Zhang W, Markfort C D and Porté-Agel F 2013 *Boundary-Layer Meteorol.* **146** 161–179
[7] Barthelmie R J and Jensen L E 2010 *Wind Energy* **13** 573–586
[8] Churchfield M J, Lee S, Michalakes J and Moriarty P J 2012 *J. Turbu.* **13** N14
[9] Stoll R and Porté-Agel F 2006 *Water Resour. Res.* **42.1** W01409
[10] Porté-Agel F, Wu Y T and Chen C H 2013 *Energies* **6(10)** 5297–5313
[11] Wu Y T and Porté-Agel F 2015 *Renewable Energy* **75** 945–955
[12] Smagorinsky J 1963 *Mon. Weather Rev.* **91** 99–164
[13] Porté-Agel F, Meneveau C and Parlange M B 2000 *J. Fluid Mech.* **415** 261–284
[14] Porté-Agel F 2004 *Boundary-Layer Meteorol.* **112** 81–105
[15] Wu Y T and Porté-Agel F 2011 *Boundary-Layer Meteorol.* **138** 345–366
[16] Albertson J D and Parlange M B 1999 *Water Resour. Res.* **35** 2121–2132
[17] Abkar M and Porté-Agel F 2013 *Energies* **6** 2338–2361
[18] Orszag S A 1970 *J. Atmos. Sci.* **27** 890–895
[19] Canuto C, Hussaini M, Quarteroni A and Zang T 1988 *Spectral Methods in Fluid Dynamics* (Springer)
[20] Monin A and Obukhov M 1954 *Tr. Akad. Nauk SSSR Geophiz. Inst.* **24** 163–187
[21] Moeng C 1984 *J. Atmos. Sci.* **46** 2311–2330
[22] Stoll R and Porté-Agel F 2009 *J. Atmos. Sci.* **66(2)** 412–431
[23] Stull R 1988 *An introduction to boundary-layer meteorology* (Kluwer Academic Publishers, Dordrecht)
[24] Businger J A, Wyngaard J C, Izumi Y and Bradley E F 1971 *J. Atmos. Sci.* **28** 181–189
[25] Wu Y T and Porté-Agel F 2013 *Boundary-Layer Meteorol.* **146** 181–205
[26] Deardorff J W 1974 *Boundary-Layer Meteorol.* **7** 81–106
[27] Tseng Y H, Meneveau C and Parlange M B 2006 *Environ. Sci. Technol.* **40** 2653–2662
[28] Abkar M and Porté-Agel F 2012 *J. Turbul.* **13** 1–18
[29] Sescu A and Meneveau C 2014 *Q. J. R. Meteorol. Soc.*
[30] Abkar M and Porté-Agel F 2015 *J. Renewable Sustanable Energy* **7** 013121
[31] Gryning S E, Batchvarova E, Brümmer B, Jørgensen H and Larsen S 2007 *Boundary-Layer Meteorol.* **124** 251–268
[32] Iungo G V and Porté-Agel F 2014 *J. Atmos. Oceanic Technol.* **31** 2035–2048